Geometry effect of isolated roughness on boundary layer transition investigated by tomographic PIV

Ye, Qingqing; Schrijer, Ferdinand; Scarano, Fulvio

DOI
10.1016/j.ijheatfluidflow.2016.05.016

Publication date
2016

Document Version
Accepted author manuscript

Published in
International Journal of Heat and Fluid Flow

Citation (APA)
Ye, Q., Schrijer, F., & Scarano, F. (2016). Geometry effect of isolated roughness on boundary layer transition investigated by tomographic PIV. *International Journal of Heat and Fluid Flow*, *61*(Part A), 31-44. https://doi.org/10.1016/j.ijheatfluidflow.2016.05.016

Geometry effect of isolated roughness on boundary layer transition investigated by tomographic PIV

Qingqing Ye[a, *], Ferry F. J. Schrijer[a], Fulvio Scarano[a]

[a] *Faculty of Aerospace Engineering, Delft University of Technology, Kluyverweg 1, Delft 2629HS, the Netherlands*

Abstract

Boundary layer transition over isolated roughness elements is investigated in the incompressible flow regime using tomographic PIV. Four different geometries (cylinder, square, hemisphere and micro-ramp) are considered maintaining constant height and span of the element. The main target is to compare the different flow topologies and study the effect of the element shape on accelerating boundary layer transition. The measurement domain encompasses the full transition process until the turbulent regime is established. The flow behavior is described by means of vortex topology and by statistical analysis of the velocity fluctuations. The instantaneous flow topology elucidates the mechanism of transition along its stages. A main distinction is observed between the bluff front elements that induce a horseshoe vortex due to upstream flow separation, leading to more rapid transition and the slender micro-ramp, requiring significant longer distance for transition onset. The mechanism of sideward propagation of the turbulent non-turbulent interface features a continuous convection and generation of hairpin-like vortices and remains the common denominator among all elements considered.

Keywords: Boundary layer, transition, roughness element, geometry effect, tomographic PIV, vortical structures

---

1. Introduction

Roughness induced boundary layer transition is an active research topic due to its significance for aerodynamic and aero-thermodynamic performance. A roughness element with large enough size acts as source of disturbance for a developing laminar boundary layer, which may greatly modify the transition mechanism and accelerate the transition process (Schneider, 2008). The roughness element induces streamwise vortices in the wake region (Rizzetta and Visbal, 2007). The former vortex structure leads to spanwise and wall-normal variations of the boundary layer flow, with the formation of low- and high-speed streaks (Fransson et al., 2004) and detached shear layer. Inflection points of the velocity profile in both spanwise and wall-normal directions are susceptible to inviscid instabilities. The phenomenon is similar to bypass transition where large freestream disturbances penetrate the boundary layer and trigger low- and high-speed streaks through a 'lift-up' mechanism (Landahl, 1990). With large enough amplitude, the streamwise streaks will undergo secondary instability and later breakdown to turbulence (Andersson et al., 2001; Reshotko, 2001).

The effectiveness of a roughness element in promoting transition strongly depends not only on Reynolds number (Tani, 1969) and roughness size (Ergin and White, 2006), but also on its shape (Klebanoff et al.,

---

* Corresponding author. *E-mail address*: q.ye-1@tudelft.nl.

1992), as different vortical patterns can be introduced in the wake, which modulate the amplitude and distribution of velocity streaks.

The flow pattern around different types of isolated roughness elements has been investigated in both subsonic and supersonic flows. Acarlar and Smith (1987) observed the periodical shedding of hairpin vortices in the separated shear layer behind a hemispherical element using flow visualization techniques. They concluded that the shear layer instability and related hairpin vortices play a significant role in the process towards transition. The self-sustained vortex shedding was also observed in the wake of a cylinder (Choudhari and Fischer, 2005). Furthermore, Ergin and White (2006) performed measurements in the wake of an array of cylinders by means of hot-wire anemometry in subsonic flow for various Reynolds numbers. They found that beyond a critical value of the Reynolds number, the induced velocity fluctuations undergo transient growth, leading to transition. Due to the good agreement between the inflection point location in the velocity profile and the location of maximum velocity fluctuation intensity, they concluded that the fluctuations leading to transition are ascribed to Kelvin-Helmholtz (K-H) instability and associated hairpin vortex structures. In a recent numerical investigation on cylinders, Loiseau et al. (2014) identified a system of counter-rotating streamwise vortices in the wake of a roughness element, transporting low- and high-momentum fluid, giving rise to the streamwise velocity streaks. Moreover, a global stability analysis indicates that both a K-H instability induced varicose mode and a streaky instability induced sinuous mode are sustained in the wake. The selection of the dominant mode leading to transition appears to be strongly dependent upon the aspect ratio of the cylinder. In a supersonic laminar boundary layer, where the roughness induced transition mechanism is particularly relevant, Subbareddy et al. (2014) used direct numerical simulation (DNS) to study the wake of a cylinder, in which a counter-rotating streamwise vortex system was also visualized. They found that the source of unsteadiness, including the effect of the upstream vortex system, shock-induced disturbances and the shear layer instability downstream of the element, highly depends upon both Mach and Reynolds number. In the wake flow over a rectangular roughness element, De Tullio et al. (2013) also observed the development of streamwise vortex pairs. In their study, the varicose instability mode shows a faster growth rate than the sinuous one, indicating a dominating effect of three-dimensional shear layer instability on the transition process. Recently, Ye et al. (2016) conducted tomographic PIV measurements over a micro-ramp at supercritical Reynolds number in an incompressible flow, highlighting the details of the mean and instantaneous flow topology. Two dominant pairs of counter-rotating streamwise vortices emanating from the micro-ramp trailing edge are observed. The evolution of the K-H vortices is captured in the instantaneous flow undergoing a fast distortion process with apparent decay before transition occurs. Instead, the interaction of secondary and tertiary streamwise vortex pairs initiates transition close to the wall, forming large scale hairpin-like vortices.

Although numerous research efforts have been devoted to the topic, the discussion remains open regarding which aspect of the roughness geometry is of primary importance in its effectiveness in promoting transition. Most studies dealing with this topic have been conducted directly in the most relevant high-speed regime (Danehy et al., 2009; 2010). For supersonic and hypersonic flight vehicle, the promotion of transition by surface roughness leads to dramatic augmentation of surface heating, which makes critical requirement for the design of thermal protection system. Tirtey et al. (2011) experimentally studied the surface footprint of the mean flow structure induced by different roughness elements (cylinder, square, micro-ramp and hemisphere) using oil-flow visualization and infrared thermography. In general, multiple pairs of streamwise vortices were identified in the wake, which persist downstream and induce secondary vortex structures propagating sidewise, which is considered as the onset of a turbulent wedge. The streamwise evolution of the surface heat transfer in the wake of different roughness elements was compared, revealing that the square shape is the most efficient in promoting transition, whereas the micro-ramp shows the lowest efficiency. By performing DNS of a supersonic boundary layer, Choudhari et al. (2009); (2010) observed the low- and high-speed streaks in the

`

roughness wake (cylinder, square, and micro-ramp) distributed periodically in the wake-span. In the stability analysis, they clarified that both streaky instability and shear layer instability coexist. Which instability mechanism dominates the transition process depends on the roughness size, shape and Reynolds number.

The present study puts the attention to the transition process in the low-speed regime, where compressibility effects do not play a role and the topology of the flow can be studied in its details to determine the transitional flow pattern. Four different isolated roughness geometries (cylinder, square, hemisphere and micro-ramp) are considered with the main objective of comparing the early stages of transition. The experimental investigation makes use of tomographic particle image velocimetry (PIV), which depicts the velocity and vorticity field in a three-dimensional domain. The measurement domain covers a large streamwise range till the onset of the turbulent flow regime in order to follow the evolution of vortical structures along the complete transition process. The experiments are conducted at a supercritical roughness height based Reynolds number (Re_h = 1170). The cross-flow topology identifies the mean structure of streamwise vortices embedded in the near wake. The statistical evaluation of the velocity fluctuations yields the distinction between the turbulent and laminar flow regions. The details of unsteady flow activity are inspected by instantaneous visualization with the aid of the vortex detection λ_2 criterion. The main findings are summarized and visually elucidated with conceptual sketches of the streamwise vortices organization and the occurrence of hairpin-like vortices.

2. Experimental Configuration and Flow Conditions

The experiments were conducted in the open jet low-speed wind tunnel at the Aerodynamic Laboratory, Delft University of Technology. The wind tunnel has an exit cross section of $0.4\times0.4\text{m}^2$, which follows the contraction that has a ratio of 9:1. A smooth aluminum flat plate with a length of 700mm, span of 400mm and a thickness of 10mm is positioned along the mid-plane of the test section. In order to prevent flow separation at the nose, the leading edge of the plate was designed with a super elliptic profile (Lin et al., 1992). Black-matt adhesive foil covers the plate to avoid unwanted laser light reflections.

The roughness elements (cylinder, square, hemisphere and micro-ramp, as schematically shown in Fig. 1) with a height (h) of 2mm and span width (c) of 4mm were oriented along the centerline at 290mm downstream from the leading edge. The length (l) of micro-ramp was 4.5mm, resulting in an incidence angle (β) and half sweep angle (α) of 24˚. The x, y, z axes of the coordinate system correspond to the streamwise, wall-normal and spanwise direction respectively. The origin of the coordinate system (o) is located at the wall, at the center of the roughness elements.

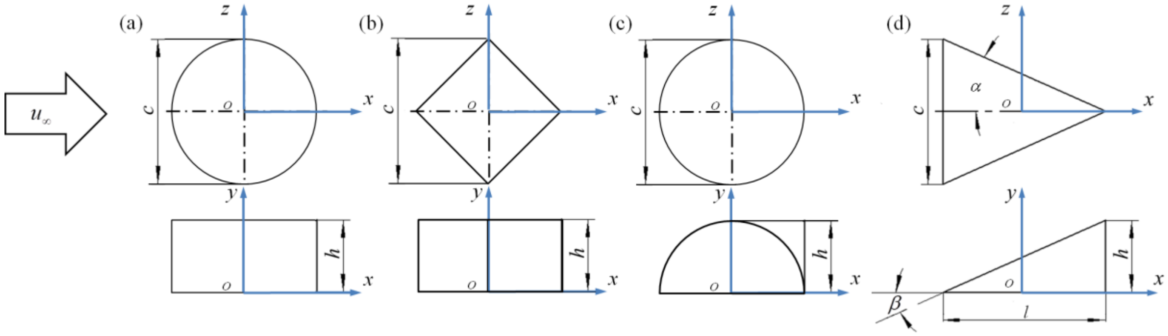

Fig. 1. Geometry of the roughness elements, (a) cylinder, (b) square, (c) hemisphere, (d) micro-ramp.

The experiments were carried out at a free stream velocity of 10m/s. The corresponding Reynolds number based on roughness-height ($Re_h=u_h\times h/\upsilon$) is 1170. Based on the roughness h/c value of 0.5, the critical Re_h ranges from 455 to 682, indicating a supercritical condition for the current experiment (Klebanoff et al., 1955; Von Doenhoff and Braslow, 1961). The undisturbed boundary layer thickness (δ_{99}) is 3.26mm at the roughness location. The resulting ratio between roughness height and boundary layer thickness is $h/\delta=0.61$. Finally, the shape factor is 2.59, indicating that the incoming boundary layer is in the laminar regime.

The tomographic PIV system features four LaVision Imager Pro LX interline CCD cameras (4872×3248pixels, 7.4μm/pixel) arranged along an arc subtending an angle $\beta = 60^\circ$ (Fig. 2). Nikon objectives of 105mm focal length are mounted at an angle to comply with the Scheimpflug condition. The aperture was set at $f_\#=11$, resulting in a focal depth of 8.4mm. The flow was seeded with a SAFEX fog machine that generates water-glycol droplets of approximately 1μm diameter. The seeding concentration is carefully adjusted at approximately 4 particles/mm^3. The measurement region was illuminated with a dual-pulse Quantel *CFR PIV-200* Nd: YAG laser (200mJ/pulse, 532nm wavelength, 9ns pulse duration). The laser light is directed from the back of the model. A sharp illumination edge is realized with a knife-edge filter installed at the trailing edge of the plate (Fig. 2). The pulse separation time was set to 30μs, yielding a particle displacement of 10pixels in the free stream. The active sensor size is 4872×1500pixels, corresponding to a measurement volume size of 145(x)×6(y)×45(z)mm^3 (72.5h×3h×22.5h). As a result, a digital image resolution of 33.6pixel/mm (corresponding to 35.4voxel/mm) is obtained. The measurement domain originates from 5mm (2.5h) behind the center of the roughness element. Each dataset consists of 200 uncorrelated instantaneous measurements, acquired at 1.5Hz.

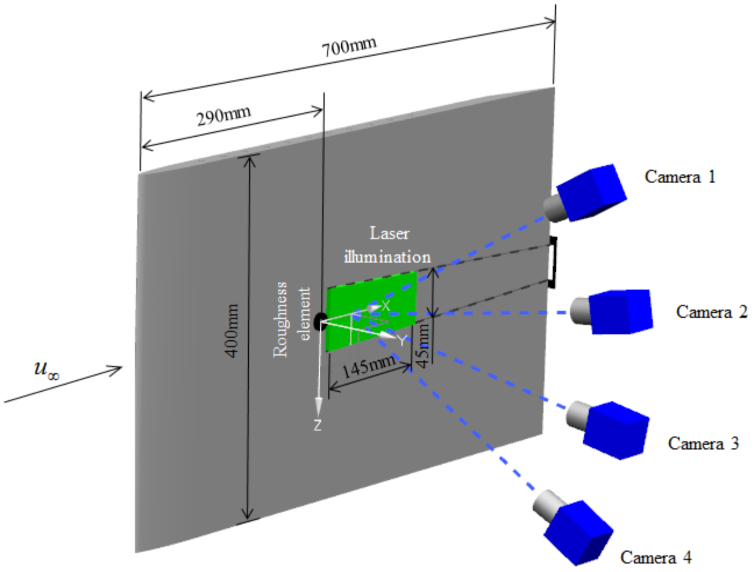

Fig. 2. Schematic representation of measurement setup.

LaVision Davis 8 was used for system synchronization, image acquisition and data processing. A 3mm thick custom-made calibration target was used for the physical calibration to establish the relation between object space and image space. The latter was further refined with the 3D self-calibration technique (Wieneke, 2008), until the vector disparity was reduced to less than 0.1pixels. The raw images were pre-processed by the

`

subtracting of time-minimum pixel intensity and of the spatial minimum over a kernel of 31×31 pixels. Image intensity was homogenized by normalization against the local average (kernel of 51×51 pixels). The measurement volume was reconstructed by using the CSMART algorithm which is similar to SMART (simultaneous implementation of multiplicative algebraic reconstruction techniques) (Atkinson and Soria, 2009). Volume correlation was based on 3D spatial cross-correlation with multi-grid and volume deformation analysis using a custom software (FLUERE) (Lynch, 2015) until a final interrogation volume of 40×20×40voxels ($1.13\times0.56\times1.13mm^3$), with an overlap of 75% between neighboring interrogation windows. The resulting spatial resolution enables the detection of vortex structure down to approximately half the roughness height. Outliers were removed by using the normalized median filter following Westerweel and Scarano (2005).

The experimental error is dominated by the uncertainty arising from the tomographic PIV measurement. The detailed uncertainty analysis was reported in the previous study (Ye et al., 2016). The uncertainty on the mean flow velocity and the RMS of velocity fluctuations are 0.7% and 0.5% of free-stream velocity (u_∞) respectively.

The development of the undisturbed boundary layer profile on the flat plate is measured and compared with the theoretical solution based on Blasius self-similarity, yielding a good agreement until the most downstream region of the measurement domain (x/h = 70). A detailed discussion can be found in Ye et al. (2016), from which Fig. 3 is reproduced.

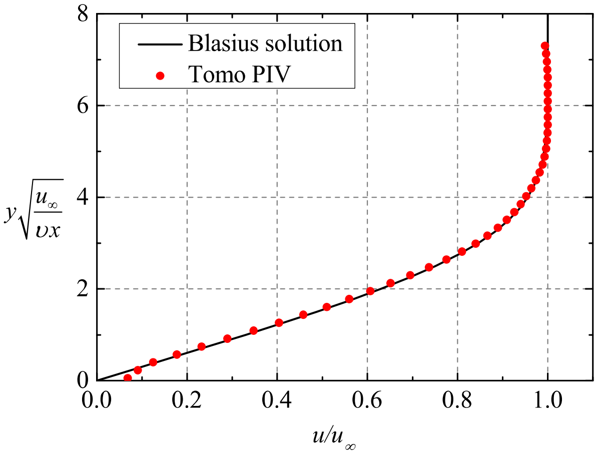

Fig. 3. Undisturbed boundary layer at x/h = 70 and comparison with Blasius solution (Ye et al., 2016).

3. Near Wake Flow Topology

The mean flow velocity and vorticity fields over different roughness elements are used to describe the near wake flow topology. The result is obtained by the ensemble average of 200 uncorrelated instantaneous snapshots. The cross-flow field is inspected at three y - z planes positioned downstream of the roughness elements (x/h = 5, 14 and 24), as shown in Fig. 4. The projected streamlines on y - z plane are visualized with the color contours of streamwise velocity (u/u_∞).

The near wake flow pattern behind the cylinder at x/h = 5 (Fig. 4(a-1)) is dominated by a pronounced counter-rotating vortex pair (*horseshoe pair*, HP) away from the symmetry plane (z/h = ±1.5, y/h = 0.3). The spanwise distance between the vortices is 3h. This vortex pair is assumed to be the trailing part of a horseshoe vortex originating from the separated region upstream of the cylinder (Baker, 1979; Hu et al., 2015). The vortex wraps around the roughness element and bends downstream, resulting into two streamwise counter-rotating vortices. The conceptual flow organization associated to the horseshoe vortex is visualized with the aid of a simplified sketch in Fig. 5(a) (dark blue line). Going back to Fig. 4(a-1), lateral upwash motions are produced by the horseshoe vortices, which induce low-speed regions and evident velocity deficits at z/h = ±2.0. In the back of the cylinder, another reversed flow region induces a weaker pair of counter-rotating vortices (*rear pair*, RP) which push low momentum flow upwards, giving rise to a low-speed region around the symmetry plane. A saddle point is formed at y/h = 0.6. Downstream at x/h = 14 (Fig. 4(a-2)), the horseshoe orginated vortices move upward to y/h = 0.6, while the spanwise location of the vortex core remains unaltered. A tertiary pair of vortices (*tertiary pair*, TP) is formed, which are located to the outside of the HP vortices. The whole vortex system generates five saddle points and alternating low- and high-speed regions. Further downstream at x/h = 24 (Fig. 4(a-3)), an additional vortex pair (*fourth pair*, FP) of even weaker vorticity magnitude is identified due the mutual induction effect of the neighbouring vortices, producing an increased number of saddle points together with the aforementioned vortical structures. The overall active area of the wake flow propagates in both wall-normal and spanwise direction. A simplified model of the flow pattern in the near wake of cylinder is sketched in Fig. 5(a), where the multiple counter-rotating streamwise vortex pairs are visualized with dark blue, light blue, purple and pink lines. The induced low- and high-speed regions are highlighted with grey and yellow projections on the wall.

Similar to the vortical structure downstream of the cylinder, the horseshoe vortex pair (HP) is also present downstream of the square at x/h = 5, as shown in Fig. 4(b-1) and the conceptual sketch in Fig. 5(b). The spanwise separation of the trailing vortices is 3.6h, slightly larger than that behind the cylinder. The latter may be ascribed to the increase in effective frontal area as the front sides of the square induce a further lateral expansion of the separated shear layer. The development of the vortex system with secondary and tertiary vortex pairs appears to be simpler than for the cylinder. The velocity deficit close to the symmetry plane is relatively weak, no clear circulation observed and the RP vortices are barely observable (shown with the dashed blue line in Fig. 5(b)). Compared with the cylinder, the tertiary vortex pair (TP) makes its appearance at a more upstream location at x/h = 5. Travelling downstream, besides wall-normal movement, the HP vortices also propagate slightly in spanwise direction to z/h = ±2.0 and ±2.3 at x/h = 14 and 24 (Fig. 4(b-2) and (b-3)) respectively. The wake flow shows a larger area of streamwise vortical activity (see Fig. 5(b)).

In the near wake of the hemisphere at x/h = 5 (Fig. 4(c-1)), the HP vortices exhibit a notably smaller spanwise separation (2h), inducing two low-speed regions by the action of a lateral upwash motion. Different from the vortical structure in the wake of the cylinder and square, a pair of counter rotating vortices (*trailing-edge pair*, TRP) close to the symmetry plane with rotating direction opposing to the HP can be observed at y/h = 1. The TRP vortex is postulated to emanate from the tip region of the hemisphere (see Fig. 5(c)). It produces a central upwash motion such that a velocity deficit region is induced. Moving downstream, the TRP lifts up with a rapid decrease of its intensity and becomes indistinguishable at x/h = 24 (Fig. 4(c-3)). As a result, the velocity deficit is also rapidly recovered. The mutually induced tertiary (TP) and fourth (FP) vortex pair can be detected at the side of the HP vortices close to the wall from x/h = 14 and 24 respectively. The overall area dominated by the activity of streamwise vortices is smaller compared with that of the cylinder and the square element. Note that close to the symmetry plane, the RP cannot be inferred from inspection of the streamtraces, although the streamwise vorticity field (not present in the current paper) indicates its weak presence.

The flow topology in the near wake of the micro-ramp differs from the other roughness elements, as it is simpler and more concise. Full details are also available in (Ye et al., 2016). The main difference is given by the absence of any HP vortex, due to the slender leading edge of the micro-ramp which create very weak or no recirculation region upstream of the element. Only a pair of counter rotating vortices produce a central upwash and lateral downwash motion at x/h = 5 (Fig. 4(d-1),). This vortex pair originates from the trailing edge of the micro-ramp (TRP) (Babinsky et al., 2009), as shown in the conceptual sketch in Fig. 5(d) and it

`

induces a mushroom-shaped velocity deficit region at the symmetry plane. A saddle point is formed at approximately y/h = 0.2 (highlighted as a grey dot), below which the flow is directed towards the wall. Downstream at x/h = 14 and 24 (Fig. 4(d-2) and (d-3)), a second pair of vortices (SP) appears beneath the trailing-edge pair with opposing rotating direction after the latter structure has moved upwards under the self-induced motion. The central downwash motion induced by the secondary vortex pair transports high momentum fluid downwards below the saddle point, leading to a high speed region (yellow shadow in Fig. 5(d)). Meanwhile, due to the lateral upwash motion, low-speed regions with relatively smaller velocity deficit start to form at the side of the secondary pair, where an inflectional velocity profile builds up.

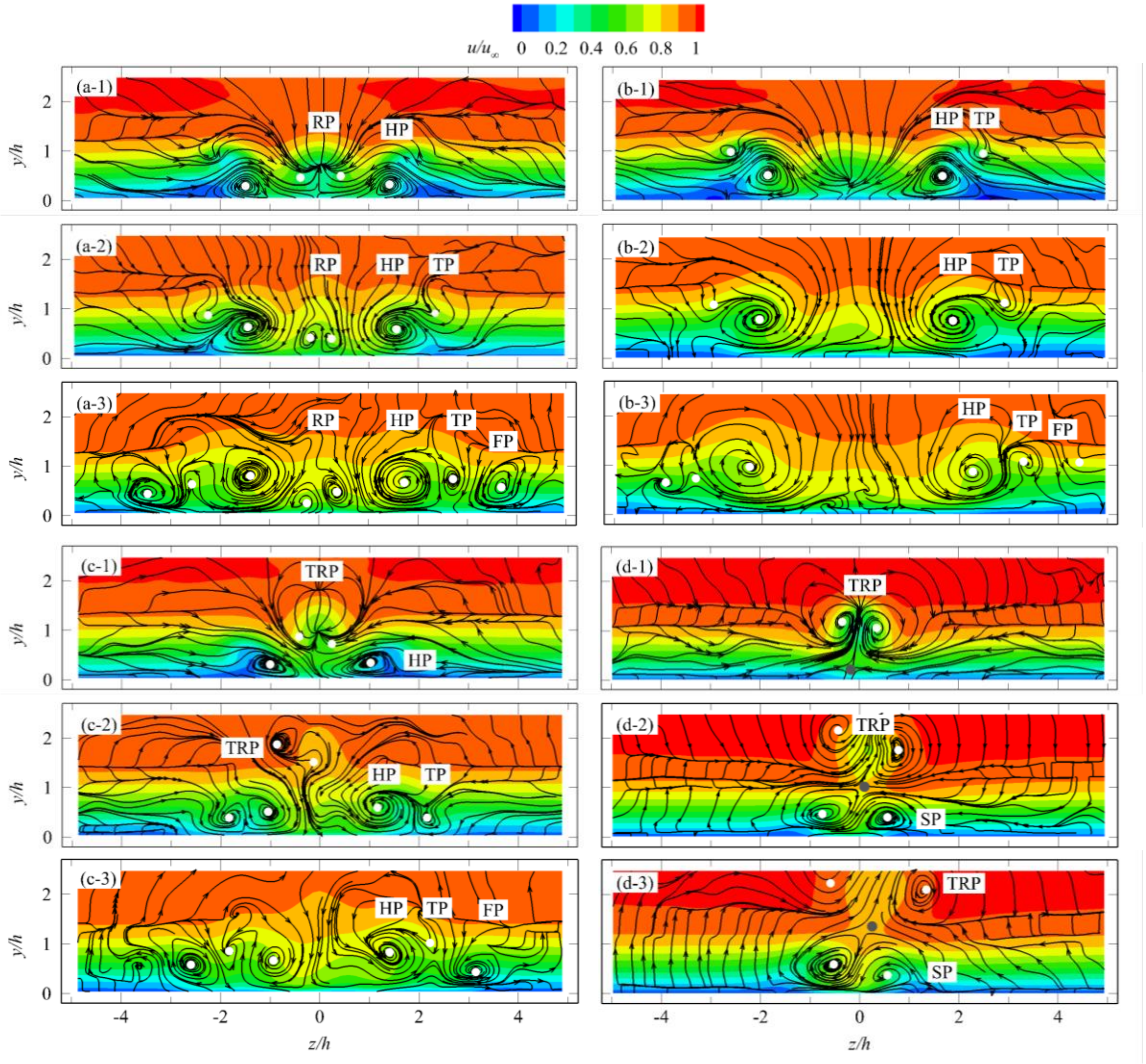

Fig. 4. Color contours of time-averaged streamwise velocity (u/u_∞), superimposed with projected streamlines at three streamwise positions: (1) x/h = 5; (2) x/h = 14; (3) x/h = 24. Results for the four geometries: (a) cylinder; (b) square; (c) hemisphere; (d) micro-ramp. (HP) horseshoe pair, (RP) rear pair, (TP) tertiary pair, (FP) fourth pair, (TRP) trailing-edge pair, (SP) secondary pair. White dots: time-averaged streamwise vortex cores, grey dots: saddle points

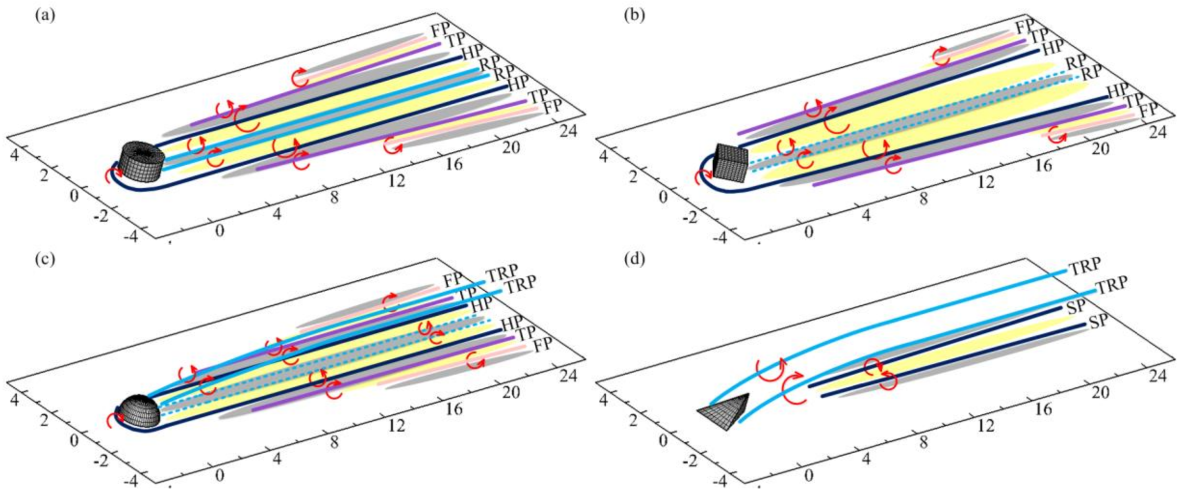

Fig. 5. Conceptual sketches of the wake topology behind different roughness elements. The solid and dashed lines are streamwise vortices; Grey and yellow projections on the wall indicate low- and high-speed regions respectively.

The occurrence of velocity streaks is one of the main features of the spanwise inhomogeneity of the flow past the roughness element, which shows a strong resemblance to the scenario of bypass transition (Brandt et al., 2004). The importance of such inhomogeneity can be quantified by the streak amplitude (Andersson et al., 2001), defined as:

$$Au(x) = \frac{1}{2}[\max_{y,z}(u(x,y,z) - u_{bl}(x,y,z)) - \min_{y,z}(u(x,y,z) - u_{bl}(x,y,z))] \qquad (1)$$

where $u_{bl}(x, y, z)$ is the velocity of the undisturbed boundary layer. After its introduction, the streak amplitude has also been used to describe the evolution of the flow property in the wake of roughness element (De Tullio et al., 2013). As shown in Fig. 6, after a slight increase in the near wake region, the streak amplitude generally decays when moving downstream. The maximum streak amplitude for cylinder, square, hemisphere and micro-ramp are 40%, 39%, 34% and 41% of the freestream velocity u_∞ respectively. As suggested in the work of Andersson et al. (2001), for a streak amplitude of $0.26u_\infty$ the sinuous mode associated to the spanwise high-shear becomes unstable (streaky instability). Instead, for a streak amplitude larger than $0.37u_\infty$, the varicose mode resulting from three-dimensional shear layer instability dominates over the sinuous mode. Accordingly, except for the hemisphere, the maximum streak magnitude of the other three roughness elements are above the upper-critical streak amplitude of $0.37u_\infty$, indicating the potential amplification of both sinuous and varicose modes close to the roughness. In the near wake of the hemisphere, the sinuous mode is assumed to dominate the growth of unstable waves. Moving downstream, the streak amplitude rapidly reduces below the upper-stability-limit ($0.37u_\infty$) from x/h = 8 for cylinder and square, and x/h = 11 for micro-ramp. Further downstream, the streak amplitude of the cylinder, square and hemisphere reach a plateau at x/h = 40, 30 and 40 of around $0.26u_\infty$, $0.28u_\infty$ and $0.26u_\infty$, respectively. In the case of the micro-ramp, the streak amplitude decreases monotonically until the most downstream region, resulting in a magnitude of approximately $0.26u_\infty$. The minimum streak amplitude of all cases remains above or approaches the lower-amplitude-limit of $0.26u_\infty$ for the growth of the sinuous mode. Consequently, the streaky instability is postulated to dominate the growth of unsteadiness in the downstream region of roughness wake.

`

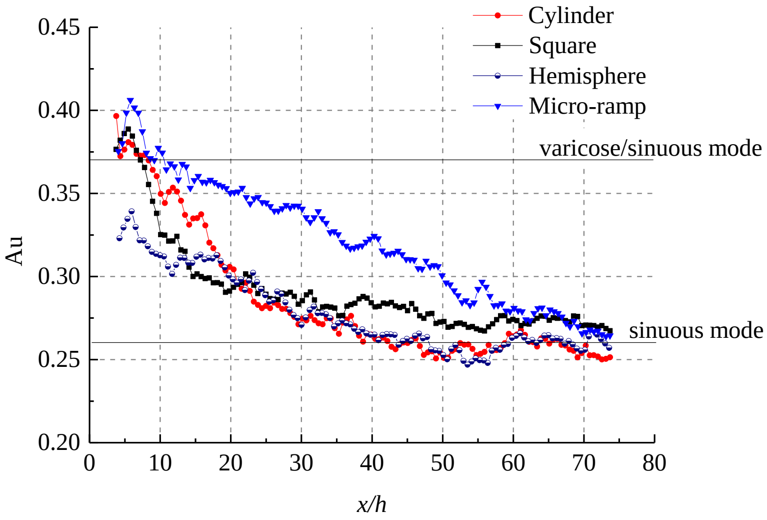

Fig. 6 The streamwise evolution of streak amplitude (Au).

4. Velocity Fluctuations

The roughness elements induce up and downwash motions in the wake, resulting in low- and high-speed regions. The increased level of shear produced in the wall-normal directions and the additional shear in the spanwise direction accelerate the growth of unstable waves, resulting in the formation of individual vortices that involve velocity and vorticity fluctuations. In order to study these, the RMS fluctuations of the streamwise velocity component ($<u'>/ u_\infty$) are extracted at six *y* - *z* cross-sections, namely *x/h* = [5, 14, 24, 35, 50, 70] (Fig. 7). The *y* - *z* cross-sectional contours are superimposed on the time-averaged streamwise velocity contour lines (u/ u_∞).

In the near wake of the cylinder, the peaks of streamwise velocity fluctuations (I, II and III) (*x/h* = 5, Fig. 7(a-1)) are concentrated at the edge of a central low-speed lobe and two symmetrical side-lobes. The inflectional velocity profile (*u* - *y*) and a high level of flow shear are produced due to the central and lateral upwash motion induced by RP and HP, which introduce unstable conditions for laminar flow development. The magnitude of the central and lateral peaks is $0.12u_\infty$ and $0.09u_\infty$ respectively. Moving downstream, due to the wake recovery process, the shear rate at the inflectional point close to the symmetry plane decays. As a result, the magnitude of peak I decreases rapidly (less than $0.10u_\infty$ at *x/h* = 14, Fig. 7(a-2)), until a peak can no longer be observed from *x/h* = 24 onwards (Fig. 7(a-3)). The downwash motion produced by the horseshoe originated vortex pair (HP) transports high momentum flow towards the wall, resulting in high near-wall shear. Consequently, an increased level of streamwise velocity fluctuations close to the wall is observed (Fig. 7(a-2) and (a-3)).

Away from the symmetry plane, the inflectional points at the upper shear layer produced by the combined effect of the horseshoe originated (HP) and tertiary vortices (TP) remain present and contribute to the persistence of the sideward velocity fluctuation peaks (II and III, at *x/h* = 14 and 24, Fig. 7(a-2) and (a-3)). A noticeable magnitude increase of peaks II and III can be observed when moving downstream. The area showing significant velocity fluctuations spreads rapidly in the spanwise direction at this stage, denoting the onset of a turbulent wedge. Peaks II and III are considered to sustain the cascade of velocity fluctuations, giving rise to laminar to turbulent transition. Unlike the relatively homogeneous distribution of streamwise velocity fluctuations at the center of a turbulent wedge (corresponding to a fully turbulent core (Schubauer and Klebanoff, 1956; Zhong et al., 2003)), two symmetrical peaks at the turbulent-non-turbulent interface of the turbulent wedge remain active till the most downstream region, indicating their role in the propagation of turbulent fluctuations towards the surrounding laminar boundary layer. A detailed analysis based on the instantaneous vortical structures contributing to the maxima of velocity fluctuations is presented in Section 5.

Compared to the cylinder, similar turbulent structures can be observed in the near wake of the square and hemisphere, with triple peaks of velocity fluctuations (peaks I, II and III at *x/h* = 5, Fig. 7(b-1) and (c-1)), located at the interfaces of three velocity deficit regions and the freestream. Compared to II and III, peak I shows the largest magnitude of $0.13u_\infty$ and $0.11u_\infty$ for the square and hemispherical element, respectively. For the square element, peak I undergoes a faster decaying process, and can be barely observed at *x/h* = 14. In the wake of the hemisphere, besides the decrease in amplitude, peak I moves upward when travelling downstream under the action of the trailing-edge vortex pair. On the other hand, the side peaks (II and III) produced by the upwash motion of the horseshoe and tertiary vortex pair persist downstream and even increase their intensity while relatively homogeneous conditions are established in the region inside the turbulent wedge.

The scenario observed in the wake of micro-ramp differs significantly from the previous three cases. Here, at *x/h* = 5 (Fig. 7(d-1)), a single peak of velocity fluctuations (I) with a relatively high intensity ($0.22u_\infty$) is detected at the detached shear layer where an inflection point is induced by central upwash motion of the trailing vortex pair (TRP) causing the occurrence of Kelvin-Helmholtz vortices (see section 5.3). The intensity of such peak decreases moving downstream, along with the central low-speed region undergoing a rapid decay. Nevertheless, the maximum can be traced until *x/h* = 30 before it disappears.

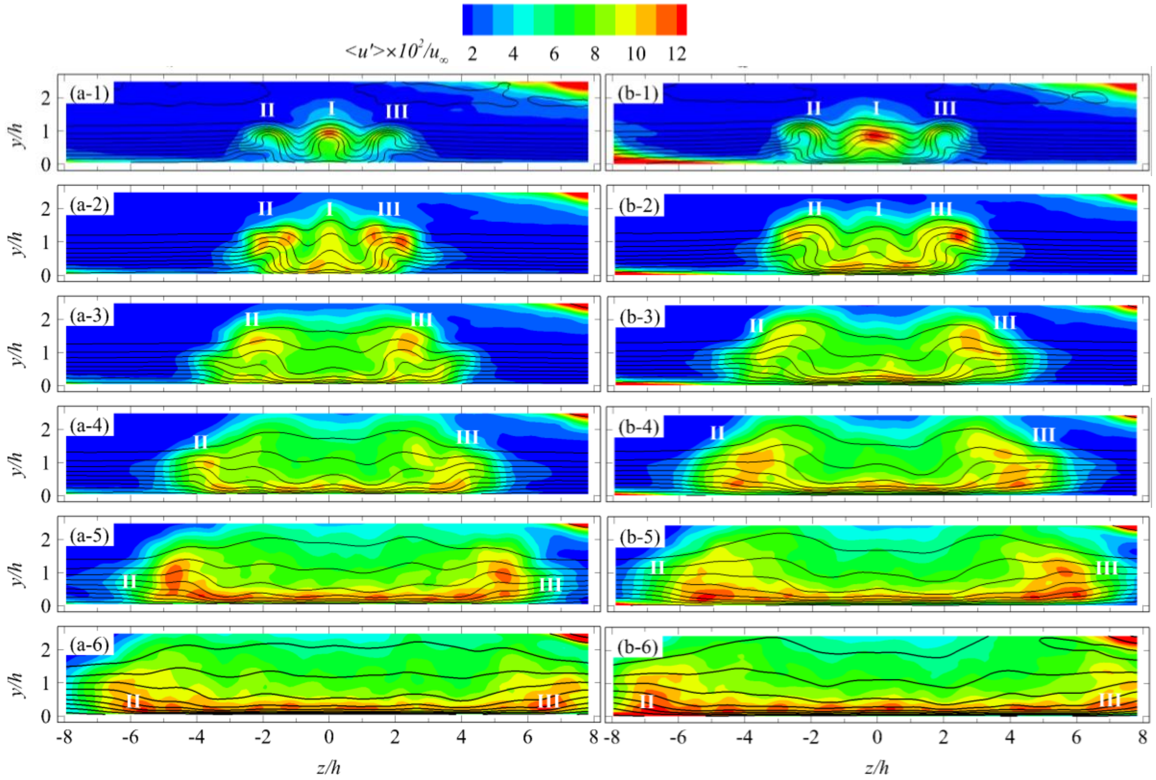

`

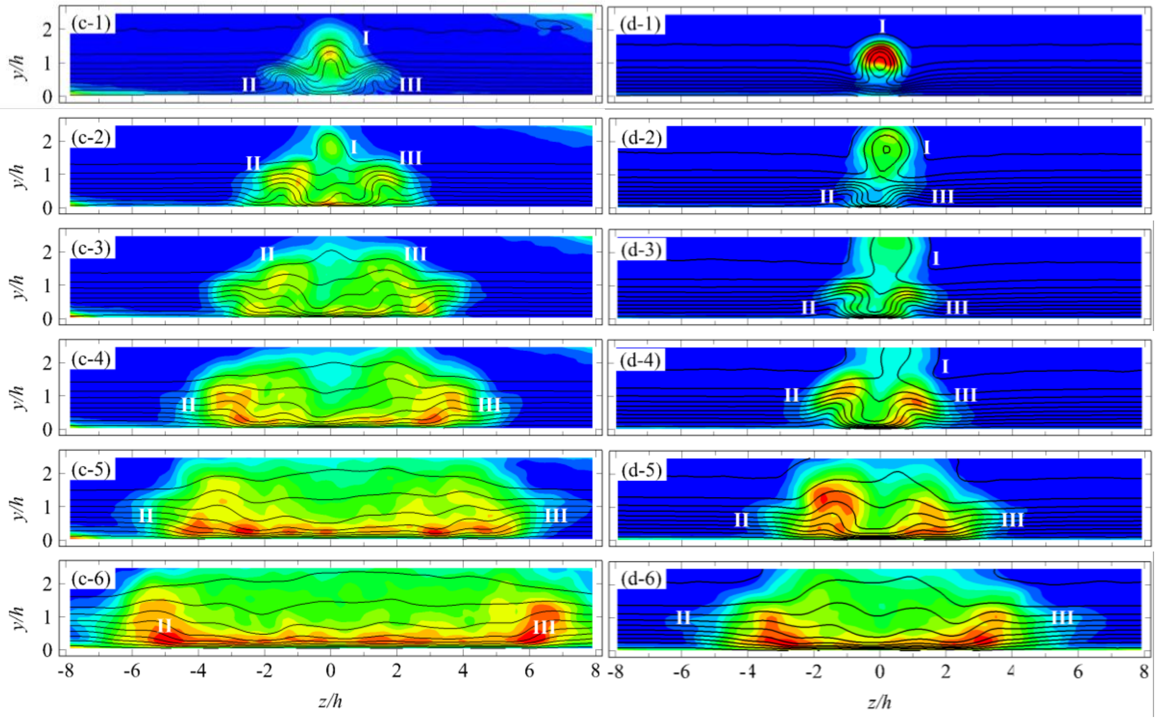

Fig. 7. *y* - *z* cross-sectional contours of streamwise velocity fluctuations $<u'>/u_\infty$, superimposed with contour lines of streamwise velocity u/u_∞; 1: *x/h* = 5, 2: *x/h* = 14, 3: *x/h* = 24, 4: *x/h* = 35, 5: *x/h* = 50, 6: *x/h* = 70; (a) cylinder, (b) square, (c) hemisphere, (d) micro-ramp.

As the wake of the micro-ramp does not exhibit any horseshoe vortex system, the flow close to the wall is not destabilized directly at the position of the roughness element, but additional vortices need to develop before critical conditions are reached that destabilize the laminar regime.

Beneath the wake region at *x/h* = 14 (Fig. 7(d-3)), the central downwash motion produced by the secondary vortices (SP) transport high momentum fluid close to the wall, resulting in high wall shear and an increased level of velocity fluctuations. The SP later induces a tertiary pair of counter-rotating vortices (TP). The upwash motion induced jointly by SP and TP contributes to the formation of two sideward low-speed regions and inflectional velocity profiles (*u* - *y*). The overall result features the inception of the sideward velocity fluctuation peaks (peaks II and III in Fig. 7(d-2)), similar to those observed for the other roughness elements. However, in this case, the process is significantly postponed (approximately 20 roughness heights).

The formation of the turbulent wedge indicates that the late stage of transition occurs in the wake of all considered roughness elements. The spreading angle of the turbulent wedge evaluated from the present observation domain yields a slightly lower angle for the micro-ramp (4.6°) and slightly larger value for the square element (6.4°). The cylinder and the hemisphere exhibit a spreading angle of 5.5° and 5.2° respectively. The latter results are in fair agreement with a number of recently reported results converging around 6° (Singer, 1996; Strand and Goldstein, 2011; Brinkerhoff and Yaras, 2014).

5. Instantaneous Flow Organization

The onset of oscillatory motions and their growth is only represented by the time-averaged amplitude of velocity fluctuations statistics in the previous section. The dynamical characterization of the flow in relation to transition and breakdown to turbulence requires the inspection of the evolution of the coherent structures that contribute to a high level of velocity fluctuations. The present measurements allow the inspection of the instantaneous vortex organization, detected by the λ_2 criterion (Jeong and Hussain, 1995). The most prominent length scales and wavenumbers can be inferred from this analysis. The iso-surface of λ_2 is color-coded by the streamwise velocity to better discriminate between regions of accelerated and decelerated flow. The approximate location of the time-averaged streamwise vortex cores is indicated by purple lines to ease the interpretation of the flow organization. Movies (1 to 4) of 10 uncorrelated snapshots are available, showing the perspective view of the instantaneous flow pattern.

5.1. Wake flow downstream of the cylinder and square

The wake of the cylinder and square exhibits a similar mean vortex topology as well as instantaneous flow pattern. Therefore only the instantaneous flow organization over cylinder is analyzed in detail for the sake of conciseness (see Fig. 8). From the most upstream region (x/h = [3, 5]), the primary hairpin vortex (PHV) is visible at the location of the unstable separated shear layer close to the symmetry plane, originating from the K-H instability, as shown in Fig. 8(a). The initial interval of neighboring PHV is λ/h = 3.5. Downstream, at x/h = 9, the upwash motion away from the symmetry plane produced by the HP vortices and associated ejection events give rise to the formation of vortices located at the spanwise side of the convected PHV (see Fig. 8(b)). Instead of a complete hairpin vortex structure, the sidewise hairpin vortices (SHV) feature a cane or leg shape, which is caused by non-uniform stretching, partial tearing, cutting and connecting (Guezennec et al., 1989). The SHV occur in a periodic manner with the wavelength of λ/h = 1.7 (half of the initial wavelength of PHV). The SHV moves slightly in the spanwise direction when travelling downstream. The head portion of PHV and SHV contributes to the peaks of velocity fluctuations (I, II and III, Fig. 7(a)). The PHV and SHV exhibit a good degree of spanwise symmetry as the vortices appearing on the sides seem to have the same phase. This phenomenon could be explained as a process of a phase locking of the vortex system. Strong ejection events (Q2, $u' < 0$, $v' > 0$, visualized by the iso-surface of $u'v'/u^2_\infty = -0.002$, colored green) at the leg and upstream region of the head of PHV lift up the low momentum flow, inducing an inflectional velocity profile and unstable shear layer. The local inflectional profile and associated unstable behavior leads to the formation of new hairpin-shape rollers (sub-PHV) at x/h = 11 (Fig. 8(b)) between two neighboring PHV with lower vorticity magnitude. A similar regeneration mechanism of hairpin vortices was also observed in direct numerical simulations of a turbulent spot (Singer and Joslin, 1994; Brinkerhoff and Yaras, 2014) and experimental visualization of a transitional boundary layer (Guo et al., 2004). In the range of x/h = [9, 14], a spanwise-symmetrical vortex packet is formed comprising two neighboring PHV, sub-PHV and SHV. The vortex packet resembles the structure of U-shaped vortices, as proposed by Singer and Joslin (1994) and Guo et al. (2010) which consists of multiple hairpin and quasi-streamwise vortices (Fig. 8(b)), indicating the late stage of transition.

Moving downstream (from x/h = 20), the PHV loses coherence and periodicity as they appear to being distorted and break up into patches of vorticity. Later on, a similar breakdown process also occurs for the SHV. A good correspondence is observed between the spatial distribution and appearance of hairpin vortices and the low-speed regions in the time-averaged flow field. The situation is schematically depicted in the conceptual model describing the instantaneous organization of the vortical structures in Fig. 9. The PHV and

`

SHV enclose the successive low-speed regions, which are produced by the time-averaged counter-rotating streamwise vortex pairs (Fig. 5(a)), whereas, in the high-speed regions, no evident vortical activity is detected.

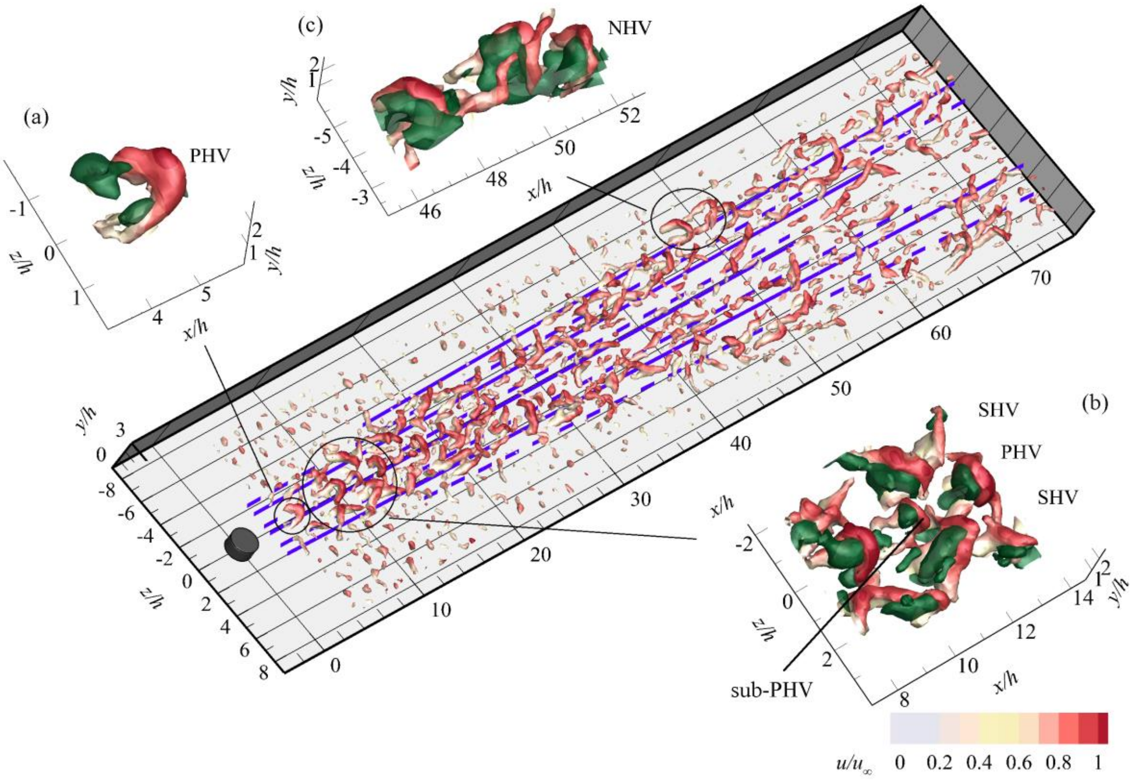

Fig. 8. The instantaneous flow pattern of the cylinder wake visualized by the λ_2 criterion, color coded by u/u_∞; Solid and dash dot purple lines: clockwise and anti-clockwise rotating streamwise vortices; the ejection event shown with green iso-surface of $u'v'/u^2_\infty = -0.002$.

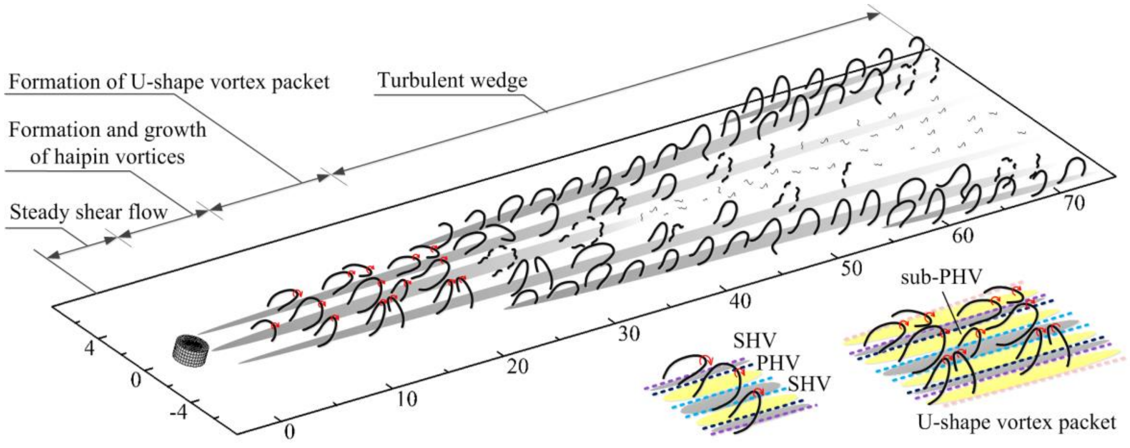

Fig. 9. Conceptual model of the transitional flow organization in the wake of cylinder; low- and high-speed regions: grey and yellow projections; dash lines: RP (light blue), HP (dark blue), TP (purple), FP (pink).

Starting from x/h = 30, a chain of newly formed hairpin vortices (NHV) can be observed with strong quasi-streamwise hairpin legs aside the SHV (see Fig. 8(c)). The new hairpins of high intensity spread spanwise concentrating at the edge of turbulent wedge. In fact, due to its intermittent behavior, the streamwise location where the NHV are first detected varies significantly in a range of x/h = [14, 40] (observed over 50 snapshots, also see Movie 1). The location of NHV agrees with the stationary low-speed regions of the mean flow produced jointly by HP and TP vortices (see Fig. 9). Close to the symmetry plane, the activity of large coherent vortices is visibly weaker, indicating that the flow yields a more isotropic turbulent regime.

In the wake downstream of the square (see Fig. 10), the PHV evolves with a smaller initial wavelength of $\lambda/h = 2.5$ and SHV exhibit half the latter wavelength. The inception of the U-shape vortex structure moves closer to the square (Fig. 10(b)). Similar to the cylinder, the NHV vortices make their first appearance in the range of x/h = [14, 40] (see Fig. 10(c) and Movie 2) and move downstream with increased concentration on the turbulent non-turbulent interface.

The transitional flow organization behind cylinder and square is summarized by the simplified model shown in Fig. 9. The short range with quasi-steady shear flow is terminated by the PHV induced disturbances close to the roughness. Moving downstream, the SHV is generated at the spanwise side of the former hairpin vortices. Later, the PHV, sub-PHV and SHV together develop into the U-shape vortex packet, indicating the late stage transition. Further downstream, the NHV develops following the border of turbulent wedge, accompanied by the breakdown process of PHV and SHV.

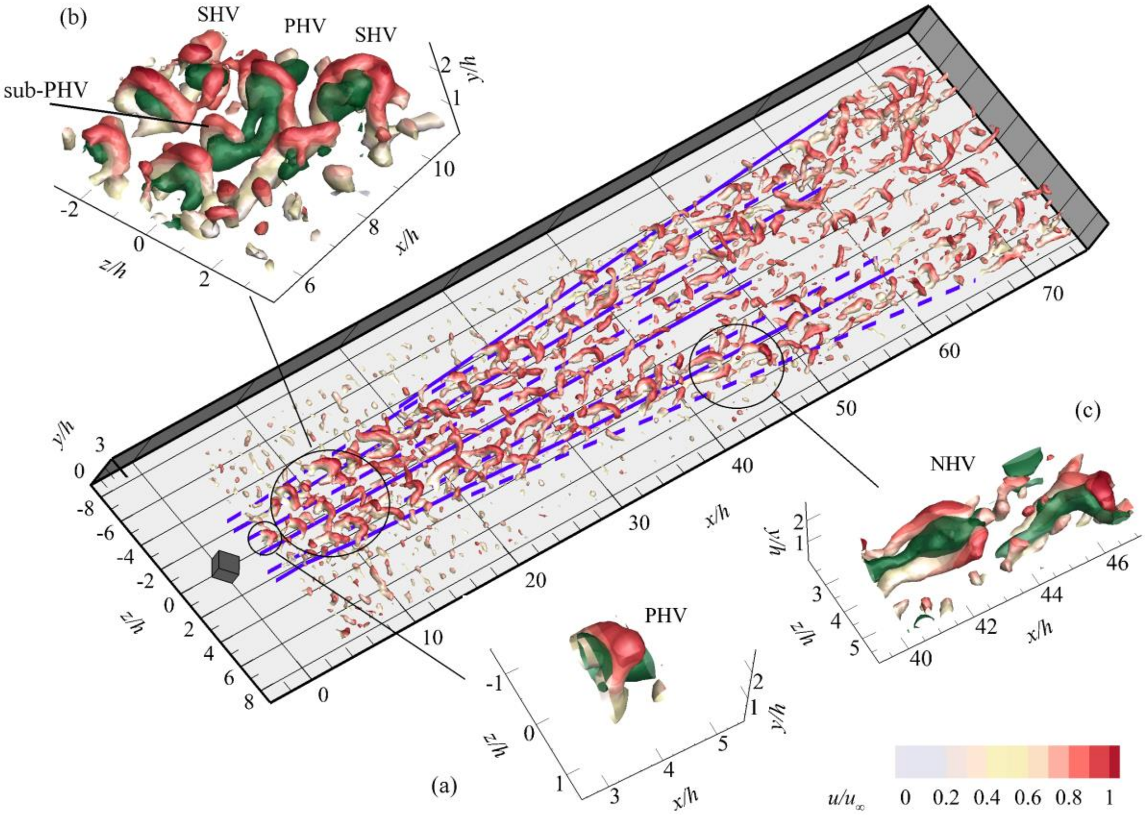

Fig. 10. The instantaneous flow pattern of the square wake visualized by the λ_2 criterion, color coded by u/u_∞; Solid and dash dot purple lines: clockwise and anti-clockwise rotating streamwise vortices; the ejection event shown with green iso-surface of $u'v'/u^2_\infty = -0.002$.

`

5.2. Wake flow downstream of the hemisphere

The primary hairpin vortices (PHV) with complete head and leg portion that shed from the hemisphere can be observed from the most upstream region in the measurement domain. The head portion of the PHV contributes to the strong velocity fluctuations at the upper shear layer (corresponding to peak I, Fig. 7(c)), where a central low-speed region produced by the upwash in the mean flow is enclosed. The initial wavelength of the PHV is 2.5*h*, which is the same as that of square. At the spanwise sides of the PHV, SHV are produced with arch-shape and a relatively lower vorticity. The SHV appear at the same location as the sideward low-speed regions. The head portion of SHV produces a high level of velocity fluctuations shown as peak II and III in Fig. 7(c).

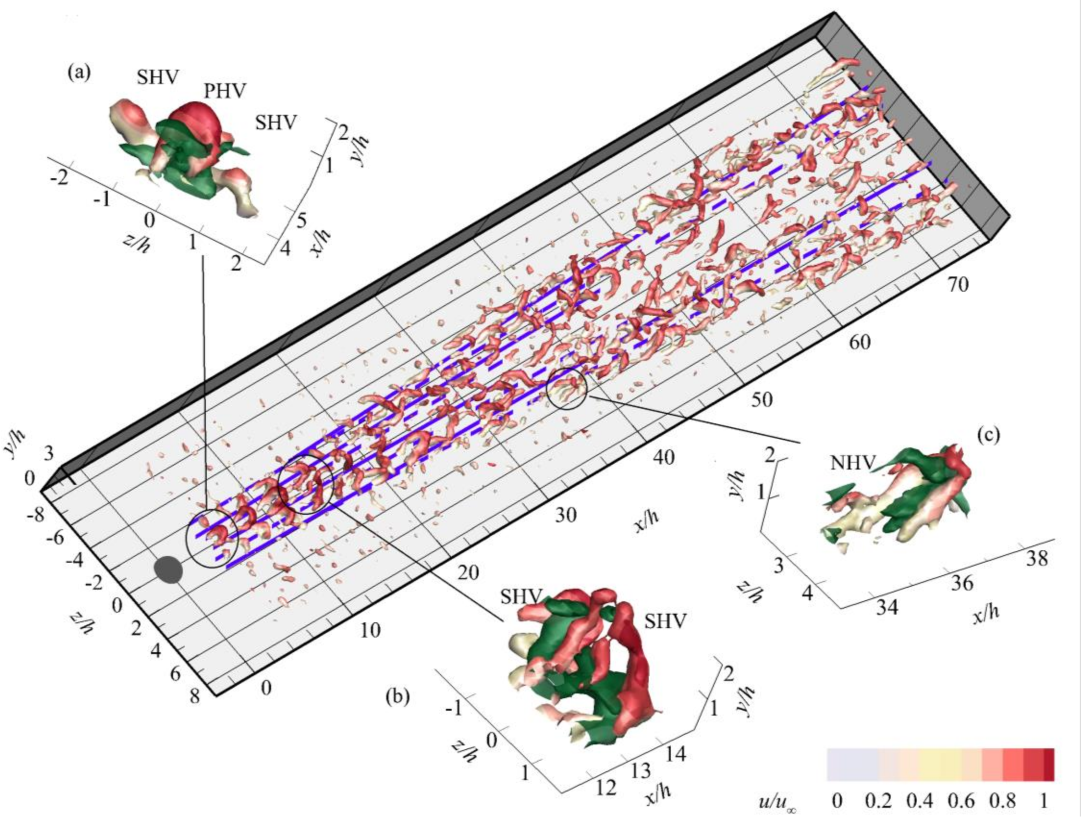

Fig. 11. The instantaneous flow pattern of the hemisphere wake visualized by the λ_2 criterion, color coded by u/u_∞; Solid and dash dot purple lines: clockwise and anti-clockwise rotating streamwise vortices; the ejection event shown with green iso-surface of $u'v'/u^2_\infty = -0.002$.

Convecting downstream, the PHV undergoes a lift-up process, in combination with a size and shape variation ascribed to vortex tilting and stretching. At x/h = [7, 10], the growth and stretching of PHV can be observed with an elongated quasi-streamwise leg portion moving close to the wall. Conversely, the head is lifted up due to the effect of a central ejection induced by the legs. The inclination angle of the hairpin is approximately 45° within this range. The wall-normal position of the hairpin head stays constant after reaching the maximum of $y/h = 2.5$, which is within the upper shear layer. Similar to the evolution of the PHV, the growing and stretching process also occurs for the SHV, which develops from an arch to a complete hairpin shape. Nevertheless, the SHV remains at a constant wall-normal position, which is similar to the relatively constant wall-normal position of the HP (see Fig. 5(c)).

When moving further downstream to $x/h = [12, 15]$, the head portion of PHV detaches from the leg and rises beyond the upper edge of the measurement domain. The whole PHV is torn apart into vortex fragments and rapidly decreases in intensity. Meanwhile, the SHV remains comparatively strong and develops following the spanwise propagation of the sidewise low-speed regions.

Starting from $x/h = 28$, the NHV appears at the side of SHV, where the fourth streamwise vortex pair (FP) starts to be active and induces low-speed regions in combination with the tertiary pair (TP) in the mean flow. The onset location of the NHV is delayed compared with cylinder and square, falling within the range of $x/h = [25, 35]$ (see Movie 3). The NHV develops downstream with a spanwise propagation, but no evident periodicity is found in the formation of these vortices. Yet, a high concentration of NHV is observed at the turbulent non-turbulent interface. In the meanwhile, the vorticity magnitude of SHV decreases due to its interaction with the growing NHV. The former vortices are later observed to be fragmented.

The conceptual model (see Fig. 12) visualizes the instantaneous vortical structure downstream of the hemisphere, where PHV shedding directly from the tip of the hemisphere. The SHV is generated bounding the PHV. Both the PHV and SHV grow downstream and undergo tilting and stretching followed by a rapid breakdown. Further downstream, the NHV is produced at the border of the turbulent wedge after the breakdown of PHV, persisting till the most downstream region. The overall instantaneous vortex pattern also resembles a wedge shape in the downstream region.

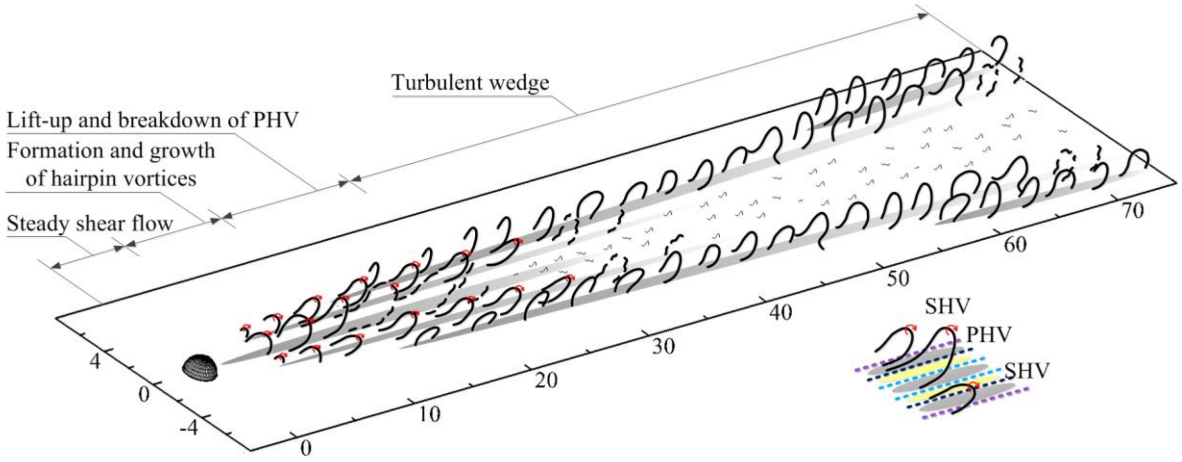

Fig. 12. Conceptual model of the transitional flow organization in the wake of hemisphere; low- and high-speed region: grey and yellow projections; dash lines: TRP (light blue), HP (dark blue), TP (purple).

5.3. Wake flow downstream of the micro-ramp

In the wake of the micro-ramp (Fig. 13(a)), Kelvin-Helmholtz rollers dominate the near wake as they are visible from $x/h = 5$ with an arc-shape (PHV) spaced at regular intervals of approximately $\lambda/h = 1.4$, which is 40% of the interval found behind the cylinder at the same flow condition. As the growth rate of the perturbation is inversely proportional to the wavelength of the vortices (Cushman-Roisin, 2014), the K-H instability is comparatively more important in the wake of micro-ramp. When convecting downstream, the vortices appear elongated and hairpin-like, due to the continuity of circulation from the head towards the legs. After the lift-up of the K-H vortices, the legs eventually connect at the bottom, forming a ring-shape. At this stage, high-speed regions are generated beneath the former vortices, corresponding to the high-speed region produced by the secondary vortex pair (SP) in the mean flow field, as shown in the conceptual model in Fig. 14. At *x/h* = 15, the interval of the K-H vortices undergoes a sudden growth ascribed to vortex pairing. As quantified by spatial cross-correlation (Ye et al., 2016), the maximum time-averaged interval of the vortices reaches $\lambda/h = 2.1$, which is only 1.5 times larger than the initial wavelength, due to the intermittent behavior observed for the pairing process.

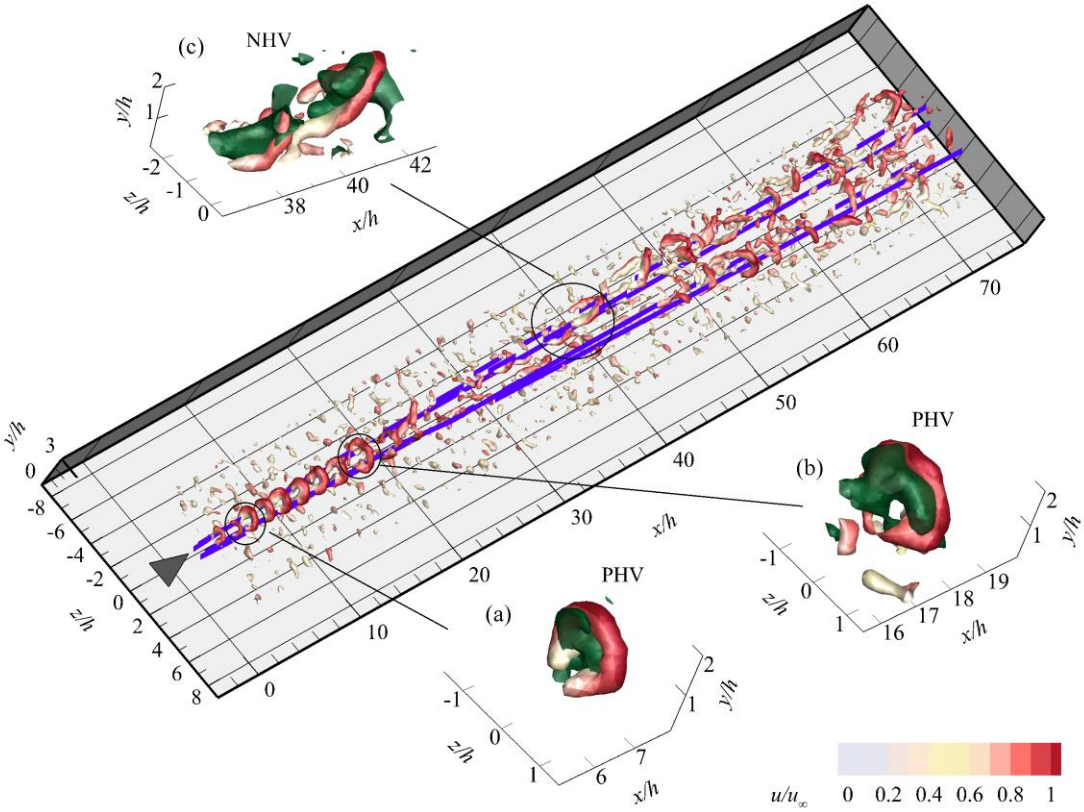

Fig. 13. The instantaneous flow pattern of the micro-ramp wake visualized by λ_2 criterion, color coded by u/u_∞; Solid and dash dot purple line: clockwise and anti-clockwise rotating streamwise vortices; the ejection event shown with green iso-surface of $u'v'/u^2_\infty = -0.002$.

After the pairing region, the PHV is observed to be distorted, splits into fragments and breaks down rapidly due to the effect of azimuthal instabilities. The vortices lose coherence and periodicity at *x/h* = 25 and show no clear pattern up until *x/h* = 35, where newly formed vortex structures (NHV) are observed in the near wall region having a hairpin shape. The inception of such hairpins is postponed to *x/h* = [30, 50] (see Movie 4). The spanwise location of NHV is the same as the sideward low speed regions. Unlike the K-H vortices close to the micro-ramp, the NHV stays at a relatively constant wall-normal position, shifting away from the symmetry plane. The location of the NHV corresponds to the turbulent non-turbulent interface, whereas no apparent activity of large-scale coherent vortex structures is observed inside turbulent wedge.

In the conceptual mode in Fig. 14, the evolution flow pattern from the micro-ramp to transition is summarized. When moving downstream, the size and shape of K-H vortices change from arch to hairpin, and in the end to a ring-shape, accompanied by lift-up, pairing and subsequently breakdown upstream of the formation of turbulent wedge. Along the side of the turbulent wedge, new hairpin vortex structures with no clear periodicity are produced.

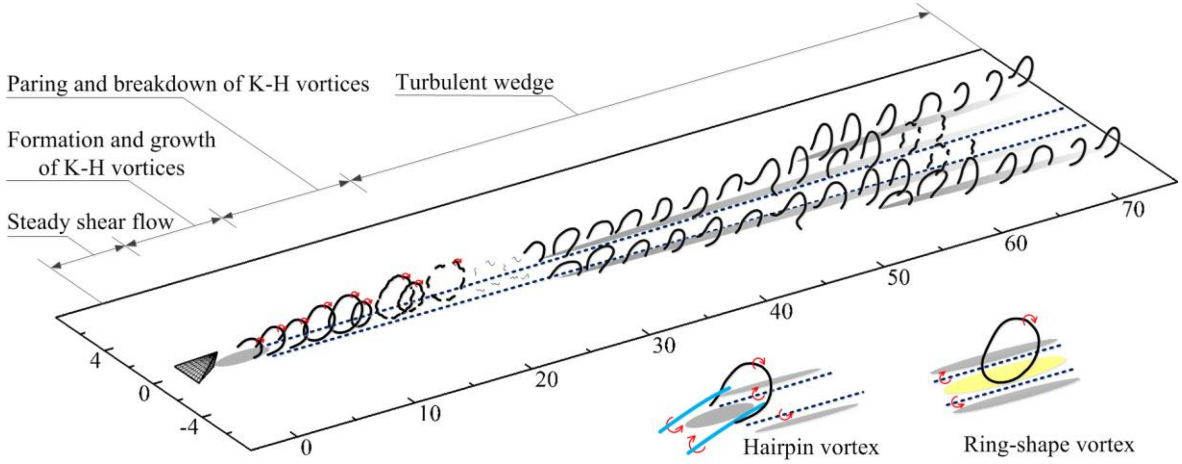

Fig. 14. Conceptual model of the transitional flow organization in the wake of micro-ramp; low- and high-speed region: grey and yellow projections; dash lines: TRP (light blue), SP (dark blue).

5.4. Features of turbulent wedge

A general evolution stage observed in the transitional flow behind the different roughness geometries is the onset of a turbulent wedge, where the late stage transition occurs. The inception of the turbulent wedge (x_w) is significantly delayed in the wake of micro-ramp compared to the cylinder and square, with an intermediate behavior for the hemisphere, revealing its geometry dependence. The features of the turbulent wedge are summarized in Table 1.

Table 1. Features of turbulent wedge

Roughness geometry	Cylinder	Square	Hemisphere	Micro-ramp
Origin (x_w/h)	[14, 40]	[14, 40]	[25, 35]	[30, 50]
Spreading angle (°)	6.4	5.5	5.2	4.6

The newly generated hairpin vortices (NHV) concentrate at the boundary of the turbulent wedge, inducing strong velocity fluctuations at the turbulent-non-turbulent interface. In the core area of the turbulent wedge, large scale coherent vortical structures are barely observed, indicating a more isotropic turbulent regime. The spanwise location of the NHV coincides with the envelope of successive low-speed regions produced by the lateral or central upwash motion of one or two neighboring streamwise vortices respectively, as presented in the time-averaged flow topology (see Fig. 4 and Fig. 5). This agreement suggests a relation between the lateral spreading of turbulent wedge and the streaky velocity distribution of the mean flow. The inception of the NHV occurs at the same location as the sideward low-speed regions. Once formed, the NHV evolve downstream following low-speed region enclosed. Further downstream, when a new low-speed region is

`

generated sideward, the inflectional instability at the newly formed high-shear layer will trigger the formation of new NHV (Krishnan and Sandham, 2006), while, the existing NHV undergo breakdown.

In summary, the spanwise propagation of turbulent wedge is assisted by the successive low-speed regions, which give rise to local inflectional instability, leading to convection and regeneration of hairpin vortices at the turbulent non-turbulent interface.

5.5. Route to transition

In the wake of all roughness elements, the rapid breakdown of PHV agrees with the decreasing level of streamwise velocity fluctuations close to the symmetry plane (peak I in Fig. 7), indicating that the perturbation at the separated shear layer induced by Kelvin-Helmholtz instability is only active in the most upstream region. The PHV loses the spatial connection with the downstream turbulent wedge in both streamwise and spanwise direction (also wall-normal direction for hemisphere and micro-ramp). As a result, the K-H instability does not play a decisive role in triggering transition.

On the other hand, the sideward low-speed regions as well as the inflectional velocity (u - y) profiles provide a favorable condition for the growth of turbulent fluctuations (Andersson et al., 2001). As a result, a cascade of NHV in the downstream region develops from the former location, indicating the onset of transition. The topological evolution from the roughness element until transition strongly depends on roughness geometry. In the wake of bluff front elements (cylinder, square and hemisphere), the horseshoe vortices (HP) become active from the most upsteam region. The lateral upwash motions induced by HP lead to the early formation of the sideward low-speed regions, which later evolve into quasi-parallel velocity streak distribution (Cherubini et al., 2013). In the case of a micro-ramp, the sideward low-speed regions are induced by secondary pair (SP). The later structure is created by the effect of excessive near-wall shear after the lift-up process of the TRP, delaying the arising of former low-speed regions. Consequently, the micro-ramp appears to be the least effective type of roughness in promoting transition when compared with cylinder, square and hemisphere.

6. Conclusion

In the present study, the three-dimensional flow organization of the boundary layer undergoing transition induced by isolated roughness elements (cylinder, square, hemisphere and micro-ramp) is investigated at a supercritical roughness-height based Reynolds number (Re_h) using tomographic PIV. It is found that the roughness geometry can greatly modify the wake flow topology and subsequently the onset location of transition.

The measurement resolution enables the detailed analysis of the time-averaged near wake flow topology. The horseshoe vortex is generated around cylinder, square and hemisphere, whose legs induce sideward low-speed regions in the wake. The inflectional velocity profiles created by the sideward low-speed regions play a key role in the inception of the flow instability and turbulent fluctuations, leading to transition. In the wake of the micro-ramp, a longer distance from the element is required for the lateral low-speed regions to develop, which are produced by the joint action of SP and TP vortices.

The evolution stage of instantaneous flow pattern from the roughness element to transition is obtained. In the downstream region, the turbulent wedge establishes with a cascade of hairpin vortex structures (NHV) concentrating at the edge, indicating the onset of transition. The inception location of NHV coincides with the sideward low-speed regions in the time-averaged flow field, which provide favorable condition for the growth of fluctuations and formation of large scale hairpin vortices. The late onset of SP as well as sideward low-speed regions in the wake for micro-ramp significantly delays the onset of transition in comparison with the case of cylinder, square and hemisphere.

The lateral spreading of the turbulent wedge is caused by a destabilizing mechanism involving the regeneration of low-speed streaks. Consequently, a general process of the convection and regeneration of hairpin vortices is observed at the turbulent-non-turbulent interface behind all the roughness elements investigated.

Acknowledgements

The work is partly funded by the Chinese Scholarship Council (CSC). The authors would like to thank Dr. Kyle Lynch for the support on data processing with the software FLUERE, Dr. Francesco Avallone and Dr. Shuanghou Deng for assisting the experiments.

References

Acarlar, M.S., Smith, C.R., 1987. A study of hairpin vortices in a laminar boundary layer. Part 1. Hairpin vortices generated by a hemisphere protuberance. J. Fluid Mech. 175, 1-41.

Andersson, P., Brandt, L., Bottaro, A., Henningson, D.S., 2001. On the breakdown of boundary layer streaks. J. Fluid Mech. 428, 29-60.

Atkinson, C., Soria, J., 2009. An efficient simultaneous reconstruction technique for tomographic particle image velocimetry. Exp. Fluids 47, 553-568.

Babinsky, H., Li, Y., Pitt Ford, C.W., 2009. Microramp control of supersonic oblique shock-wave/boundary-layer interactions. AIAA J. 47, 668-675.

Baker, C.J., 1979. The laminar horseshoe vortex. J. Fluid Mech. 95, 347-367.

Brandt, L., Schlatter, P., Henningson, D.S., 2004. Transition in boundary layers subject to free-stream turbulence. J. Fluid Mech. 517, 167-198.

Brinkerhoff, J.R., Yaras, M.I., 2014. Numerical investigation of the generation and growth of coherent flow structures in a triggered turbulent spot. J. Fluid Mech. 759, 257-294.

Cherubini, S., De Tullio, M.D., De Palma, P., Pascazio, G., 2013. Transient growth in the flow past a three-dimensional smooth roughness element. J. Fluid Mech. 724, 642-670.

Choudhari, M., Fischer, P., 2005. Roughness-induced transient growth. AIAA Paper 2005-4765, 35th AIAA Fluid Dynamics Conference and Exhibit. Toronto, Ontario Canada.

Choudhari, M., Li, F., Chang, C.-L., Edwards, J., Kegerise, M., King, R., 2010. Laminar-turbulent transition behind discrete roughness elements in a high-speed boundary layer. AIAA Paper 2010-1575, 48th AIAA Aerospace Sciences Meeting Including the New Horizons Forum and Aerospace Exposition. Orlando, Florida.

Choudhari, M., Li, F., Edwards, J., 2009. Stability analysis of roughness array wake in a high-speed boundary layer. AIAA Paper 2009-0170, 47th AIAA Aerospace Sciences Meeting including The New Horizons Forum and Aerospace Exposition. Orlando, Florida.

Cushman-Roisin, B., 2014. Environmental fluid mechanics. John Wiley and Sons, Inc, USA.

Danehy, P., Bathel, B., Ivey, C., Inman, J., Jones, S., 2009. No plif study of hypersonic transition over a discrete hemispherical roughness element. AIAA Paper 2009-0394, 47th AIAA Aerospace Sciences Meeting including The New Horizons Forum and Aerospace Exposition. Orlando, Florida.

Danehy, P., Ivey, C., Inman, J., Bathel, B., Jones, S., Jiang, N., Webster, M., Lempert, W., Miller, J., Meyer, T., Mccrea, A.C., 2010. High-speed plif imaging of hypersonic transition over discrete cylindrical roughness. AIAA Paper 2010-0703, 48th AIAA Aerospace Sciences Meeting Including the New Horizons Forum and Aerospace Exposition. Orlando, Florida.

De Tullio, N., Paredes, P., Sandham, N.D., Theofilis, V., 2013. Laminar–turbulent transition induced by a discrete roughness element in a supersonic boundary layer. J. Fluid Mech. 735, 613-646.

Ergin, F.G., White, E.B., 2006. Unsteady and transitional flows behind roughness elements. AIAA J. 44, 2504-2514.

Fransson, J.H.M., Brandt, L., Talamelli, A., Cossu, C., 2004. Experimental and theoretical investigation of the nonmodal growth of steady streaks in a flat plate boundary layer. Phys. Fluids 16, 3627-3638.

Guezennec, Y.G., Piomelli, U., Kim, J., 1989. On the shape and dynamics of wall structures in turbulent channel flow. Phys. Fluids A 1, 764-766.

Guo, H., Borodulin, V.I., Kachanov, Y.S., Pan, C., Wang, J.J., Lian, Q.X., Wang, S.F., 2010. Nature of sweep and ejection events in transitional and turbulent boundary layers. JTurb 11, 1-9.

Guo, H., Lian, Q.X., Li, Y., Wang, H.W., 2004. A visual study on complex flow structures and flow breakdown in a boundary layer transition. Exp. Fluids 37, 311-322.

`

Hu, B., Zhang, H., Younis, M.Y., Li, Y., Raza, M.S., 2015. Experimental investigation on the transition of separation/attachment in steady laminar juncture flows. Exp. Fluids 56, 1-9.

Jeong, J., Hussain, F., 1995. On the identification of a vortex. J. Fluid Mech. 285, 69-94.

Klebanoff, P.S., Cleveland, W.G., Tidstrom, K.D., 1992. On the evolution of a turbulent boundary layer induced by a three-dimensional roughness element. J. Fluid Mech. 237, 101-187.

Klebanoff, P.S., Schubauerand, G.B., Tidstrom, K.D., 1955. Measurements of the effect of two-dimensional and three-dimensional roughness elements on boundary-layer transition. Journal of the Aeronautical Sciences 22, 803-804.

Krishnan, L., Sandham, N.D., 2006. On the merging of turbulent spots in a supersonic boundary-layer flow. Int. J. Heat Fluid Flow 27, 542-550.

Landahl, M.T., 1990. On sublayer streaks. J. Fluid Mech. 212, 593-614.

Lin, N., Reed, H.L., Saric, W.S., 1992. Effect of leading-edge geometry on boundary-layer receptivity to freestream sound, in: Hussaini, M.Y., Kumar, A., Streett, C.L. (Eds.), Instability, transition, and turbulence. Springer New York, New York, NY, pp. 421-440.

Loiseau, J.-C., Robinet, J.-C., Cherubini, S., Leriche, E., 2014. Investigation of the roughness-induced transition: Global stability analyses and direct numerical simulations. J. Fluid Mech. 760, 175-211.

Lynch, K.P., 2015. Advances in time-resolved tomographic particle image velocimetry. Doctor of Philosophy Delft University of Technology

Reshotko, E., 2001. Transient growth: A factor in bypass transition. Phys. Fluids 13, 1067-1075.

Rizzetta, D.P., Visbal, M.R., 2007. Direct numerical simulations of flow past an array of distributed roughness elements. AIAA J. 45, 1967-1976.

Schneider, S.P., 2008. Effects of roughness on hypersonic boundary-layer transition. J. Spacecraft Rockets 45, 193-209.

Schubauer, G.B., Klebanoff, P.S., 1956. Contributions on the mechanics of boundary-layer transition. NACA-TR-1289.

Singer, B.A., 1996. Characteristics of a young turbulent spot. Phys. Fluids 8, 509-521.

Singer, B.A., Joslin, R.D., 1994. Metamorphosis of a hairpin vortex into a young turbulent spot. Phys. Fluids 6, 3724-3736.

Strand, J.S., Goldstein, D.B., 2011. Direct numerical simulations of riblets to constrain the growth of turbulent spots. J. Fluid Mech. 668, 267-292.

Subbareddy, P.K., Bartkowicz, M.D., Candler, G.V., 2014. Direct numerical simulation of high-speed transition due to an isolated roughness element. J. Fluid Mech. 748, 848-878.

Tani, I., 1969. Boundary-layer transition. Annu. Rev. Fluid Mech. 1, 169-196.

Tirtey, S.C., Chazot, O., Walpot, L., 2011. Characterization of hypersonic roughness-induced boundary-layer transition. Exp. Fluids 50, 407-418.

Von Doenhoff, A.E., Braslow, A.L., 1961. The effect of distributed surface roughness on laminar flow, in: Lachmann, G.V. (Ed.), Boundary Layer and Flow Control. Pergamon, pp. 657-681.

Westerweel, J., Scarano, F., 2005. Universal outlier detection for piv data. Exp. Fluids 39, 1096-1100.

Wieneke, B., 2008. Volume self-calibration for 3d particle image velocimetry. Exp. Fluids 45, 549-556.

Ye, Q., Schrijer, F.F.J., Scarano, F., 2016. Boundary layer transition mechanisms behind a micro-ramp. J. Fluid Mech. 793, 132-161.

Zhong, S., Chong, T.P., Hodson, H.P., 2003. A comparison of spreading angles of turbulent wedges in velocity and thermal boundary layers. J. Fluids Eng. 125, 267-274.